ROYAL SOCIETY OPEN SCIENCE

royalsocietypublishing.org/journal/rsos

Research

Cite this article: Bertini L, Hendy E, Summerfield R, Fernandez V, Clark B, Martin-Silverstone E, Lucka F, Kiss MB, Johnson K. 2026 How to quantify and minimise error in coral skeletal density estimates using X-ray µCT. *R. Soc. Open Sci.* **13**: 251288.
https://doi.org/10.1098/rsos.251288

Received: 8 July 2025
Accepted: 29 January 2026

Subject Category:
Ecology, conservation, and global change biology

Subject Areas:
biometrics, biogeochemistry, environmental science

Keywords:
X-ray micro-CT, coral skeletal densitometry, error analysis, protocol standardization, calibration, marine calcification

Author for correspondence:
Leonardo Bertini
e-mails: leonardo.bertini@liverpool.ac.uk; l.bertini@nhm.ac.uk

Supplementary material is available online at https://doi.org/10.6084/m9.figshare.c.8335609.

THE ROYAL SOCIETY PUBLISHING

How to quantify and minimise error in coral skeletal density estimates using X-ray µCT

Leonardo Bertini[1,2,3], Erica Hendy[2], Rebecca Summerfield[2,4], Vincent Fernandez[5], Brett Clark[4], Elizabeth Martin-Silverstone[6], Felix Lucka[7], Maximilian B. Kiss[7] and Kenneth Johnson[1]

[1]Department of Earth Sciences, Natural History Museum, London SW7 5BD, UK
[2]School of Earth Sciences, Wills Memorial Building, University of Bristol, Bristol BS8 1RJ, UK
[3]Deptartment of Earth, Ocean and Ecological Sciences, School of Environmental Sciences, University of Liverpool, Liverpool L3 5DA, UK
[4]Natural History Museum, London SW7 5BD, UK
[5]European Synchrotron Radiation Facility, 38000 Grenoble, France
[6]Bristol Palaeobiology Group, School of Earth Sciences, Life Sciences Building, University of Bristol, Bristol BS8 1TQ, UK
[7]Department of Computational Imaging, Centrum voor Wiskunde en Informatica, 1098 XG Amsterdam, The Netherlands

LB, 0000-0003-3920-4476; EH, 0000-0001-5949-4349; RS, 0009-0003-6915-4622; VF, 0000-0002-8315-1458; BC, 0000-0002-5888-9223; EM-S, 0000-0003-0139-2109; FL, 0000-0002-8763-5177; MBK, 0009-0005-0986-8361; KJ, 0000-0002-4666-1213

X-ray micro-computed tomography (µCT) is widely used in environmental and ecological studies to visualise the complex skeletons of marine calcifying organisms. However, the potential to quantify skeletal density in marine calcifiers is complicated because µCT greyscale intensities are influenced by many factors. Here we constrain sources of error in coral skeletal densitometry and show how errors can be quantified, minimised and reported. We establish the accuracy and precision of density estimates by analysing a population of massive *Porites* spp. coral that vary in bulk average skeletal density (1.07–1.57 g cm^{-3}), size (4–25 cm in diameter), mass (87.9–2176.5 g) and morphology (41 specimens scanned in 81 individual µCT acquisitions). The population mean offset between the µCT-derived density and actual values was 0.2 ± 4.6% ($\bar{x}$ ± 1 SD, n = 41). Following acquisition-specific corrections based on bulk density offsets, equivalent internal regions of low and high

density within repeatedly scanned corals under different settings varied by only ±0.8% (1 SD). We present a workflow for μCT laboratories to measure density, and minimise and report errors. Application of these recommendations will ultimately improve data comparison of coral skeletal growth assessments. The workflow recommendations are transferable to the μCT densitometry analysis of other marine calcifying organisms.

1. Introduction

For a coral reef to persist, the ecosystem must maintain a positive balance over time between carbonate deposition and loss [1]. Reef carbonate budgets can be used to assess and monitor reef status in terms of kg $CaCO_3$ m^{-2} yr^{-1} from a census of the reef organisms that calcify or erode, and abiotic processes that accrete or dissolve carbonate (e.g. [2–4]). The dominant calcifying group on modern tropical shallow water reefs is coral [5]. Any carbonate budget, therefore, relies heavily on the quality of coral calcification rate estimates [6] which in turn are calculated from the growth rate and density of skeleton deposited by coral colonies [7]. Challenges to accurately quantifying coral skeletal density include the array of skeletal structures, porosity and morphologies across taxa [8] (figure 1A). Coral can also subsume material of different densities and porosities, produced by associated organisms or the reef rock that the colony originally settled on (figure 1C). In addition, skeletal density is highly variable within populations of the same species and within individual specimens (e.g. bulk average skeletal density can vary 30–40% in a population of the dominant reef-forming massive coral *Porites* spp. from a single reef [7], >50% between reefs [9] and by ±10% within an individual colony [10]; figure 1B). The varied instrumentation, standardization, applied corrections and methodologies used to measure coral skeletal density have made it difficult to compare density and calcification rates across studies and between regions [8]. Strategies to measure coral skeletal densities from whole colonies or extracted cores include: buoyant weight techniques (liquid displacement or dry/wet weight) [11–15], two-dimensional X-ray radiography [16–22], γ-densitometry [23–27] and, increasingly, three-dimensional visualization and quantification of density using X-ray computed tomography (CT) [14,28–33]. The ability to resolve the complexity and range of internal density variation (e.g. figure 1B) is a valuable advantage of both γ- and X-ray densitometry, but these approaches require additional post-processing to convert attenuation greyscale intensities into density units. Density standards are therefore necessary, and calibration approaches have included: aluminium wedges [19,21], sub-samples of coral [29,30,33], calcite or *Tridacna* shells of independently measured density [26,27,34], and medical imaging phantoms of hydroxyapatite [14,32,35]. Despite the use of standards, CT studies of coral skeletons have reported substantial sensitivity to operator and image reconstruction decisions that remain uncorrected. For instance, DeCarlo [33] found coral skeletal density could be over-estimated by 39–44%, while Carilli *et al.* [14] reported density under-estimations of approximately 50%. The density offset corrections applied in CT densitometry studies on marine calcifying organisms are significant (approx. 12% for *Porites* spp. coral [14], 9% for coralline algae [34] and on the same scale as two-dimensional γ-densitometry 10% [15]). With the recent rapid advancements in μCT hardware and image reconstruction algorithms [36] and an expanding number of research institutions establishing μCT research facilities, there is a need for an independent test to routinely evaluate consistency and establish the accuracy and precision of measurements for reporting alongside results.

The work presented here consists of two major contributions. Firstly, we use a population of 41 *Porites* spp. specimens to quantify how different factors and decisions in μCT imaging affect the accuracy and precision of coral skeletal density estimates. Specifically, we test how sensitive the μCT density estimate is to:

(1) Specimen characteristics (e.g. morphology, mass, size and skeletal density).
(2) Calibration decisions (e.g. whether the phantom is scanned with the coral, what regression fit is used, the density range and composition of the calibration standards).
(3) Instrument set-up (e.g. warm up time and filament age) and operator decisions (e.g. X-ray tube voltage and current, filter material and thickness).
(4) Post-processing decisions such as built-in reconstruction algorithms designed to improve image quality (e.g. beam hardening correction).

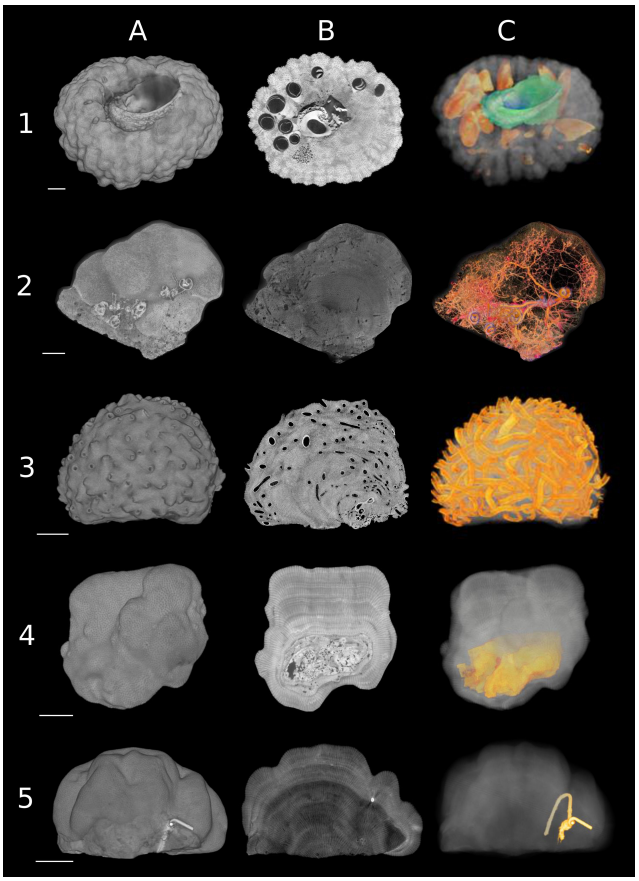

Figure 1. Examples of µCT reconstructions and density variability of internal features in colonies of massive *Porites* spp. (A) Surface views highlighting external appearance of coral and epi- and endobionts. Scale bars are 20 mm. (B) Reconstructed cross-section slices of colonies. The brighter the greyscale intensity the denser the material, demonstrating range of density from internal air pockets (black) to regions of dense calcified structures. (C) Segmented internal features highlighting different calcifiers, bioeroders and subsumed material contributing to the bulk mass of the colony as a whole. **Colony 1.** (1A) Encrusting oyster shell causing a change in coral colony morphology. (1B) Density variability of coral skeleton due to annual density banding and in response to contact with filter-feeding borers (*Lithophaga* sp.). Large round air-filled chambers containing bivalve shells (*Lithophaga* sp.) and small dissolution features created by boring sponges. The densest carbonate is the oyster shell. (1C) The full contribution from various endobionts including additional barnacles and spiral worms to the volume and mass of the whole coral colony. **Colony 2.** (2A) Spiral worms (*Spirorbis* sp.) forming high-density carbonate tubes attached to outer coral surface. Dark spots are boring sponge chambers. (2B) Complexity of internal sponge dissolution and added porosity. (2C) Full extent of internal sponge network and superimposed spiral worm complex attached to outer surface. **Colony 3.** (3A) Coral surface distortions caused by a large population of endolithic filter-feeding Christmas tree worms (*Spirobranchus giganteus*) growing in tandem with the host colony. (3B) Cross section highlighting differences in internal density from coral annual banding, the high-density outer rim of the calcifying worm tubes and the internal volume now filled with air. (3C) The dominance of the colony volume by the calcifying worm tubes and the complexity of the internal structures. **Colony 4.** (4A) Relatively featureless coral colony surface. (4B) Internal density variability due to annual high- and low-density banding. Vertically parallel high-density lines are corallite walls around individual coral polyps, which asexually divide over time, increasing the surface area of the colony. High-density reef rock, containing variably sized and shaped air pockets, contributes significantly to colony volume and mass (4B,4C) but is invisible from the external surface view (4A). **Colony 5.** (5A) A relatively featureless coral colony surface except for a protruding metal wire. (5B) Internal density variability within the coral skeleton includes a persistent increase in skeletal density over the last 2 years of colony growth, as well as annual high- and low-density banding through the 6 year lifespan of the colony. The intense bright spot is a cross section of a metal wire. On the lower right, there is a high-density scar and coral overgrowth that occurs concurrent with placement of the wire. (5C) Internal positioning and extent of wire highlighted.

Secondly, we propose concrete, easy-to-follow recommendations to establish a robust workflow for density estimation. We introduce a protocol for an independent specimen-specific 'bulk mass test' to establish the accuracy of density estimates from every acquisition. Significantly, we demonstrate that any applied corrections must be individually assessed for every acquisition. Application of these recommendations will ultimately improve data comparison of massive coral skeletal growth

assessments between researchers, laboratories and study areas. The workflow recommendations are transferable to the µCT densitometry analysis of other marine calcifying organisms.

2. Material and methods

In this section, we first introduce the sample set, µCT systems, calibration and reconstruction procedures, then we describe the protocol for calculating the '*bulk mass test*' and '*density offset*', before outlining the various experiments designed to test the sensitivity of the µCT-derived density estimates to potential sources of uncertainty.

2.1. Coral specimens

Massive *Porites* spp. are the most common coral taxa analysed for skeletal density and calcification rate data [6,37]. Forty-one air-dried *Porites* specimens were selected from collections of the Natural History Museum (NHM, UK) and the Naturalis Biodiversity Centre (NCB, The Netherlands). The diameter of individual specimens ranged from 4 to 25 cm and varied in surface rugosity, shape and internal features, including density-banding, bioerosion and secondary calcification from endobionts. We used linear mixed effects models to quantify the sensitivity of µCT density estimates to specimen size (using mass), morphology (using surface area : volume ratio) and density. Sample and dataset acquisition details are provided in electronic supplementary material, SI-1 and SI-2, respectively.

2.2. X-ray µCT systems and reconstruction procedures

Our study was performed at the NHM X-ray CT laboratory and the University of Bristol (UoB) XTM Facility using the same µCT system (Nikon XT H 225 ST), totalling 84 high-resolution (approx. 50–120 µm) X-ray µCT acquisitions. Both systems produce conical polychromatic X-ray beams, but the UoB system had a 2000 × 2000 pixel flat panel detector (200 µm pixel pitch), while the NHM system had a 2850 × 2850 pixel detector (150 µm pixel pitch). All X-ray three-dimensional volume reconstructions were carried out using Nikon's proprietary reconstruction software 'CT Pro 3D' and exported as 16-bit datasets for further processing.

2.3. Calibration standards and procedures

The 'narrow' density calibration standards are in a commissioned radiology phantom from QRM (EU offices) following the design used by Cantin *et al.* [35] and recommendations in ASTM standards (https://www.astm.org/e1935-97r19.html). The phantom contains inserts with varying concentrations of calcium hydroxyapatite (0 to 1241.9 mg cm^{-3}) in an epoxy matrix, corresponding to densities from 1.13 (epoxy: 'e') to 1.92 g cm^{-3} (insert 5 : 'i5'), and an uncertainty of ±0.5% (electronic supplementary material, figure S4, and fig. 3.2 in [38]). Greyscale intensities (i.e. X-ray attenuation) for each density standard insert in the phantom give a 'narrow' 6-point calibration range. The 'extended' 11-point calibration also included air (0.001225 g cm^{-3}; International Standard Atmosphere model value at 15°C and sea level) plus 4 additional standards attached around the outside of the QRM phantom with densities of 0.126 g cm^{-3} (sweetener: 's'), 0.260 g cm^{-3} ('coffee powder': 'c'), 0.904 g cm^{-3} (sunflower oil: 'o') and 2.70 g cm^{-3} (aluminium: Al) (see electronic supplementary material, SI-4, for shelf product specifications, empirical density measurements and attachment design). The extraction of greyscale intensities for all density standard calibration points was semi-automated and calibration relationships were calculated using the median greyscale intensity for each standard (electronic supplementary material, figure S6). As part of replicate acquisitions for the least dense, mid-range and densest coral specimens (see §2.5.1) four additional $CaCO_3$ calibration standards, two calcite (2.69 and 2.76 g cm^{-3} respectively) and two aragonite crystals (2.92 and 2.94 g cm^{-3} respectively), were included to test sensitivity of calibrations to high density material composition and heterogeneity (see electronic supplementary material, SI-6, for details and empirical measurements).

2.4. How to assess the accuracy and precision of µCT density estimates

A protocol '*bulk mass test*' was devised to assess the accuracy of a µCT density estimate for each dataset acquisition in terms of a '*density offset*'. In summary, the offset between the two independently established masses for the specimen can be expressed as a percentage:

$$Offset\ (\%) = \frac{\mu CT\ derived\ mass\ -\ actual\ mass}{actual\ mass} \times 100. \tag{2.1}$$

Ideally if a dataset acquisition is accurate, the offset (equation (2.1)) would be 0% because the modelled µCT-derived mass (or density) is equal to the actual mass (or density) of the specimen. Further, a negative offset indicates that the modelled mass estimate is lighter than the actual skeleton, whereas a positive offset means a heavier modelled result than reality. Similarly, precision of replicate acquisitions can be determined by the variance in terms of the offset (±1 standard deviation (SD)). The mass offset is numerically equivalent to a density offset if the actual and modelled specimen volumes are the same. Given that the purpose of this study is to demonstrate how to minimise errors in µCT-determined skeletal density estimates, from this point on we quantify accuracy, replicate precision and population variance in terms of the density offset.

To calculate the µCT-derived coral specimen density and mass it is first necessary to calculate the volume of the specimen. In our study, volume segmentation was conducted in Avizo 2022.2 (ThermoFisher Scientific) by human-assisted greyscale intensity thresholding through all slices of the dataset to produce a binary mask. In the experiments where specimens were repeatedly scanned to quantify precision or the impact of different operational settings, all datasets of the same colony were spatially registered, and a single reference three-dimensional volume mask applied, eliminating any variability introduced by the segmentation process (see electronic supplementary material, SI-7).

The second step is to extract a histogram of the voxel counts per greyscale intensity from the segmented volume. In our study, this dataset was exported as a .csv file and then each greyscale intensity value bin in the 16-bit histogram ('*i*th' bin from 0 to 65 535) was converted into a density estimate using the density calibration regression for the acquisition.

The mass of each individual *i*th greyscale intensity bin can be calculated across the histogram and summed to produce the '*µCT-derived mass*' of the whole specimen (equation (2.2)), where the voxel volume was obtained from the resolution of the acquisition:

$$\mu CT\ derived\ mass\ (g) = \sum_{i=0}^{i=2^{16}-1} density_i \times voxel\ count_i \times voxel\ volume. \tag{2.2}$$

The '*actual mass*' of every coral specimen was measured on a four-figure balance and the '*bulk mass test*' is the difference between the two independently established bulk masses for the whole specimen relative to the specimen's actual mass (equation (2.1)).

The accuracy and precision of µCT-derived density estimates for a population of analyses can be calculated from the population average and standard deviation of all density offsets in the sample set. This is the value to report as an evaluation of a CT laboratory's process error and determines any additional scaling correction required for the bulk density of a specific acquisition dataset. Density offset data are invaluable for laboratory monitoring and exploring how to minimise errors as well as essential for reporting the uncertainty associated with the extracted CT density data.

2.5. Experiments

2.5.1. Sensitivity to calibration decisions

Calibration and noise sensitivity were assessed for all dataset acquisitions and are presented as ±1 SD of the density offset for the whole specimen. Density estimates using the full 11-point 'extended' phantom calibration curve were compared with density estimates using the traditional 'narrow' selection of standards by excluding various standards in post-processing. This assessment was completed for the sample population of eight skeletons scanned using the UoB system and 33 using the NHM system. Further sensitivity tests involved (i) removing or adding specific density standards from the calibration (e.g. the lowest and highest density points for air and aluminium respectively) and (ii) artificially simulating greyscale noise. The estimated magnitude of scattering in air was approximately 500 greyscale intensity units which was applied to the greyscale intensity value for air to explore the

sensitivity of the calibration to this noise (see electronic supplementary material, SI-5). A range of regression fits (linear, third-degree polynomial, exponential and Gaussian) were also explored. Overall, four regression fits coupled with up to six calibration adjustments were considered (totalling up to 24 different calibration curves) per single scan depending on the phantom design used. Instrument settings were optimised for each specific specimen (electronic supplementary material, table S3). Additional replicate scans for the least dense, mid-range and densest coral specimens were carried out to test for significant differences in colony bulk density offsets between calibration choices. All data acquisitions were internally calibrated except in the following crossover experiment.

A crossover experiment was conducted to test whether scanning the specimen and phantom together in the same data acquisition ('internal calibration') yielded a different density estimate compared with datasets collected for both objects in separate acquisitions ('external' calibration). For the 'internal calibration', the phantom was centred directly above or below the coral specimen along the rotation axis to maintain the spatial homogeneity of the scan. This ensured that the phantom experienced the same beam path, scatter conditions and reconstruction geometry as the sample, allowing its known densities to calibrate greyscale values consistently throughout the three-dimensional volume. When the phantom was scanned alone it was completed during consecutive acquisitions under the same settings as the coral specimen. Six specimens with different density, morphology and size were assessed in the crossover experiment (total of 18 scans; full details in electronic supplementary material, table S4, and schematic in electronic supplementary material, figure S3).

2.5.2. Sensitivity to instrument set-up and operator decisions

During any initial set up of a scan the µCT operator will seek an optimal setting. Given the number of parameters that can be tuned, there are a wide range of possible solutions that can provide an 'optimal'-looking image. However, there is also no universal solution expected for a population of samples because of the natural density variability found internally and between specimens of the same genus (figure 1B). In this experiment, we conducted a series of acquisitions across a group of five coral specimens varying in shape, size, density and mass to quantify the impact of operational decisions on coral bulk density estimates. In total 5–9 individual scans of each specimen combined different X-ray tube voltages (140, 180 or 215–220 kV), filter materials and thicknesses (Cu 1 and 2 mm, and Sn 1 mm; see electronic supplementary material, table S3). Acceptable X-ray attenuations in the densest portions of the skeleton were monitored by checking the detector panel live-feed before initiating the scan. All scans were calibrated with the 'narrow' 6-point phantom.

Precision and potential instrumental drift in terms of the estimated colony density were assessed by three replicated scans of the same coral specimen at different times as the NHM X-ray µCT system warmed up over the same day. The scans were completed under moderate source voltage and the same filter (180 kV; Sn 1 mm) and with a new filament. A further experiment investigated reproducibility between the density measurement from a scan using a filament at the very end of its life cycle and a scan of the same specimen with a brand-new filament (in this case both scans were performed under low beam energy and efficient filtration; 140 kV, Sn 1 mm). We use the observed standard deviation to estimate the propagated error that would be associated with multiple scans to account for the compounded instrumental error if external calibration is used.

2.5.3. Sensitivity to proprietary image enhancement algorithms

It is common in CT imaging to apply additional algorithms to reconstructions of raw projection data to correct for systematic image artefacts [39–41] including patterns of streaks or shadows, scattering or randomly distributed granulated noise. One of the most common artefacts is beam hardening [42–45], which arises from the higher attenuation of low-energy photons compared with the high-energy photons when a polychromatic X-ray beam passes through particularly dense objects. This results in unusually high attenuation (greyscale intensity) in low-density regions (or thinner parts of the sample, especially towards outer edges), which can lead to erroneous density estimates. Proprietary reconstruction software typically includes optional algorithms for the reduction of artefacts and levels of correction that can be chosen based on the severity of the artefact present in the image. The impact of the proprietary Nikon beam hardening artefact corrections on the measurement of coral bulk density was assessed by applying level '2' beam hardening correction to a suite of scans from a single specimen and replicated for two specimens at either end of the population density range to confirm

observed impacts (figure 2a, purple versus orange markers). From each scan, a pair of reconstructions were produced, one with the default artefact corrections enabled and a second where all corrections were disabled (i.e. a raw reconstruction scan).

3. Results

3.1. How sensitive are µCT density estimates to specimen characteristics?

In total, 81 acquisitions were performed across 41 *Porites* spp. specimens (electronic supplementary material, table S1; experiments detailed in §2). The actual mass and density of the sample population ranged from 87.9 g to 2176.5 g, and 1.07 g cm^{-3} to 1.57 g cm^{-3}, respectively (figure 2). Ideally if a dataset acquisition is accurate, the *y*-axis offset would be 0% (see equation (2.1); §2.4) because the modelled µCT-derived mass (or density) is equal to the actual mass (or density) of the specimen. The mean density offsets for the 72 scans with internal calibration ranged from −13% to +8% and averaged 0.2 ± 4.6% ($\bar{x}$ density offset ± 1 SD; n = 41) across the population of samples in our study (figure 2a, purple and black points). Scans of less dense coral (10 out of 41 scans < 1.2 g cm^{-3}) consistently yielded µCT datasets that overestimated sample density (4.9 ± 2.0%; $\bar{x}$ density offset ± 1 SD). By contrast, modelled µCT densities were lower than actual densities for colonies with a skeletal density > 1.2 g cm^{-3} (−1.3 ± 4.1%; n = 31 coral). When split into light (<1000 g; n = 28) or heavy (>1000 g; n = 13) specimens (figure 2b), individual density, mass and therefore size were all significant factors controlling the density offset ($p < 0.001$ and $p < 0.01$ respectively; type-III ANOVA F-test, $R^2 = 0.81$), whereas surface area : volume ratio and scan resolution (i.e. voxel size) had no significant influence (see electronic supplementary material, figure S11). Additionally, the slope of the density relationship was more sensitive (i.e. significantly steeper) for heavier colonies (−21.6 ± 6.3% density offset per g cm^{-3}, $p < 0.01$) than those lighter than 1000 g (−16.3 ± 3.1% density offset per g cm^{-3}; figure 2b).

3.2. How sensitive is the µCT density estimate to calibration decisions?

The error bars plotted on the density offset data (*y*-axis, figure 2a) represent variability (up to ± 5%, 1 SD) introduced by different calibration choices. Calibration-induced variability is dependent on colony density, with less dense skeletons associated with higher sensitivity to calibration fit decisions. This variability is reduced significantly when an 'extended' phantom design is used that contains air (0.001225 g cm^{-3}) and additional low density standards, plus a high density aluminium (2.70 g cm^{-3}) calibration point instead of the 'narrow' phantom design (black versus grey point pairings in figure 2a; and further tests in figure 3a). Additionally, note how the variability in offset explained by changes in density reduced from $R^2 = 0.51$ in the narrow case to $R^2 = 0.16$ in the extended case across a larger population of scans (figure 3b,c respectively). By contrast, the addition of more high density calibration points using calcite (2.69 and 2.76 g cm^{-3}) and aragonite (2.92 and 2.94 g cm^{-3}) crystals, or in place of the Al standard, caused an increase in calibration-induced variability due to the natural heterogeneity of the minerals (electronic supplementary material, SI-6, figures S8–S10).

The difference in calibration standard range between phantom designs (6-point or 7-point 'narrow' compared with 11-point 'extended') caused a +2% to 4% mean density offset shift, depending on the specimen, with greatest impact at the extremes of the skeletal density range of the sample population (figure 2a). An 'extended' phantom design consistently pulled points towards the 0% line compared with the 'narrow' range (figure 2a, black versus grey circles, respectively). No significant difference in mean density offset was found when calcite and aragonite crystals were used as high density standards in the calibration range instead of, or in addition to, Al (electronic supplementary material, SI-6, figures S8–S10).

Employing internal calibration with an extended phantom design also minimised calibration-related variability (figure 3b,c). Externally calibrated scans (i.e. the phantom is not included in the same acquisition as the coral specimen) resulted in significantly different mean density offsets (paired $t_{(5)} = 2.58$, $p < 0.05$, n = 6 pairs) and variability ($t_{(5)} = 2.71$, $p < 0.05$) and the 'extended' phantom yielded the smallest variability and density offsets closer to 0% (figure 3a). Although internally-calibrated datasets were more tolerant of a limited calibration range (i.e. no significant differences in density offset were found for the sub-set of six coral specimens used in the crossover study; figure 3a), when the complete study population of internally-calibrated scans were compared (n = 36; black and grey points in figure

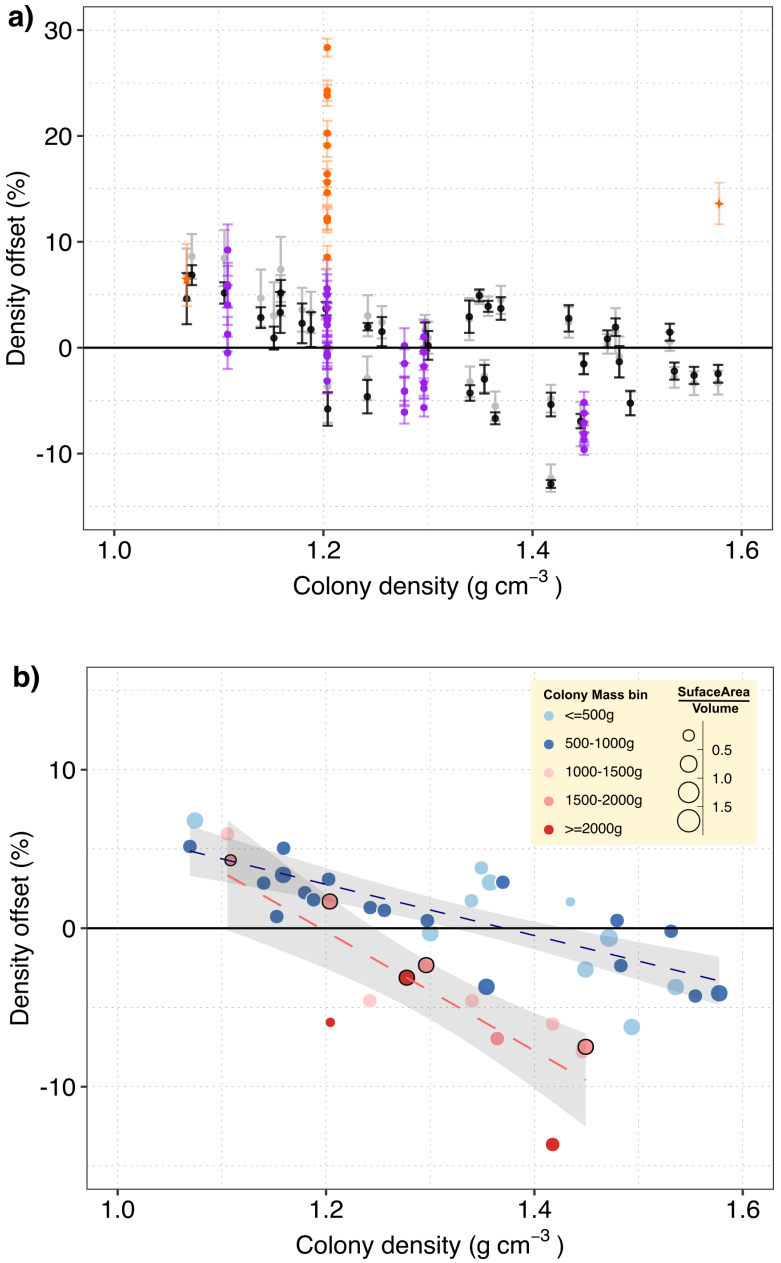

Figure 2. Density offsets (% difference between µCT-derived and actual densities) as a function of actual density for a population of 41 coral specimens. (a) Mean density offset for 72 individual scans; symbols colour-coded according to experiment. Black symbols show estimates calculated using the calibration from the 'extended' 11-point phantom; paired with grey symbols using the traditional 'narrow' (6-point) phantom design. Purple symbols show repeated scans of five individual coral under 5–9 different µCT operator-selected system settings plus replicate tests. Orange symbols show the impact of beam hardening correction applied to data acquired from a single coral under different system settings and two additional corals on either end of the density range shown as ✶ and ✦ (least dense and densest specimens, respectively). Error bars indicate variability due to calibration and noise sensitivity for each scan (±1 SD). (b) Mean density offsets for 41 coral specimens. Symbols are colour-coded by mass and size proportional to surface area-to-volume ratio of each coral specimen. Linear regression fits (dashed lines) for colonies <1 kg (blue shades) and >1 kg (red shades); grey envelopes 95% CI. Symbols with a black outline are averages of the repeated data acquisitions for the coral specimens shown by purple symbols in (a).

2a) in a pair-wise analysis between a calibration based on the narrow or extended range of standards, significantly differences were identified for both mean density offset (paired $t_{(35)} = -4.23$, $p < 0.001$) and variability (paired $t_{(35)} = -5.45$, $p < 0.001$; figure 3b,c).

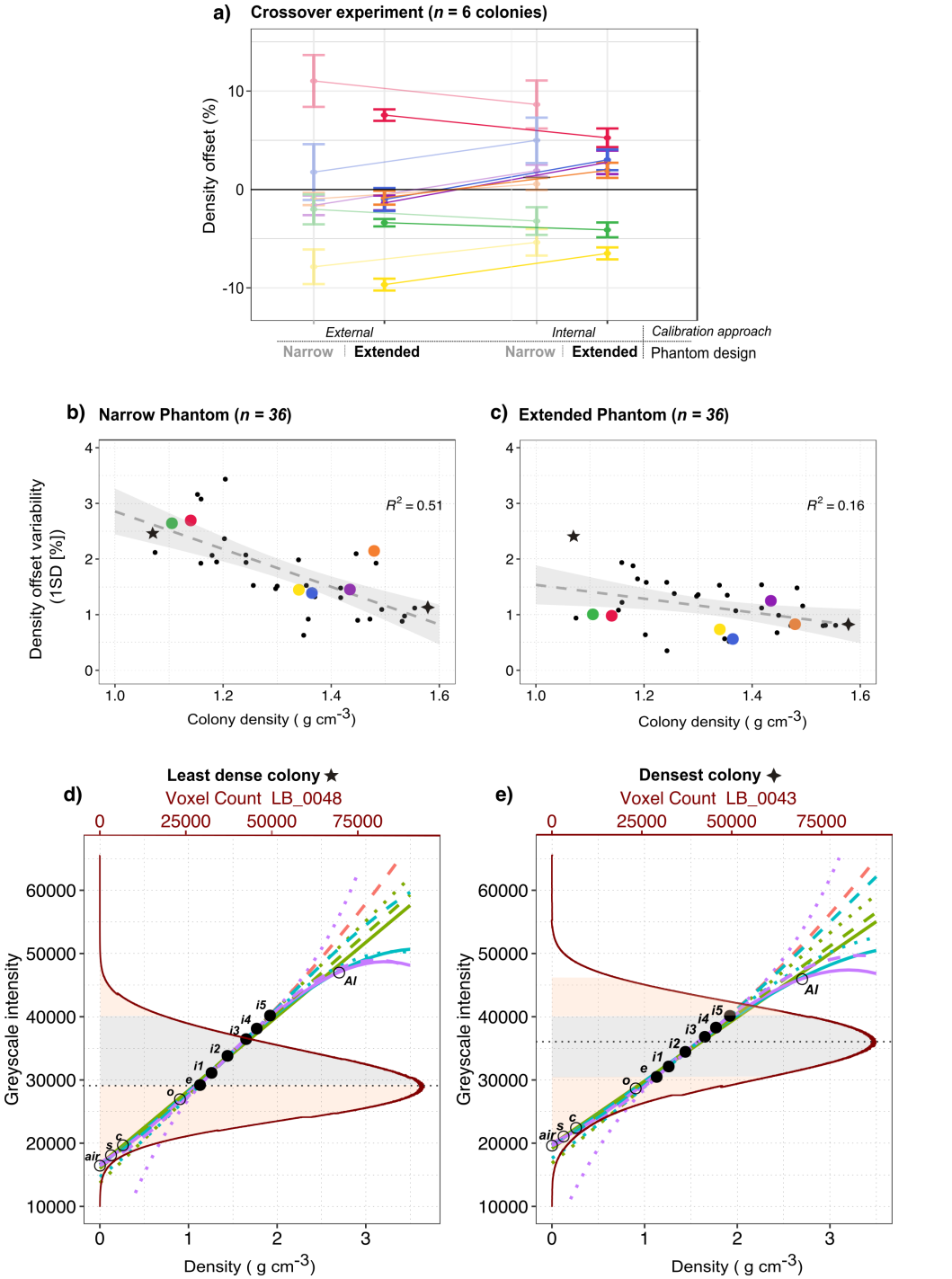

Figure 3. Sensitivity of density estimation to calibration approaches. (a) Crossover experiment to test sensitivity to the range and number of density standards ('extended' or 'narrow' phantom design), and inclusion of the phantom within the same data acquisition as the coral ('internal' versus separate 'external' calibration). Error bars indicate variability due to calibration and noise sensitivity for each acquisition (±1 SD). (b,c) Correlation between the variability introduced by calibration and noise for each dataset acquisition relative to colony density for (b) 'narrow' and (c) 'extended' phantom design with regression fit and 95% prediction envelope. Symbols for specific individual coral specimens are consistent between panels, and colours indicate the specimens used in (a). (d,e) Greyscale intensity (segmented 16-bit histogram) and range of possible calibration curves for the least dense (d) and densest (e) coral skeletons (shown as ✶ and ✦ respectively in b,c). Circles indicate density standards extracted from the traditional 'narrow' phantom (inserts i1–i5 and e 'epoxy'; filled circles) and 'extended' phantom (air, 's' for 'sweetener', 'c' for 'coffee powder', 'o' for sunflower oil and Al for aluminium; open circles). Solid lines are calibration curves (linear, third-degree polynomial, exponential and Gaussian fits) using 'extended' phantom design while dashed and dotted lines of same colour indicate 'narrow' phantom with and without air, respectively. Greyed-out (versus salmon) area under histogram shows range of greyscale intensities captured by the 'narrow' (versus 'extended') calibration standard range.

3.3. How sensitive is the µCT density estimate to instrument set-up and operator decisions?

Variability associated with instrumental reproducibility is negligible compared with that induced by other factors examined in this study. The density offsets calculated from replicated scans of the same coral varied by 0.02% (±1 SD, $n = 3$ scans) during different warm-up phases of the X-ray gun through a day. Consequently, the expected propagated analytical error associated with separate scans of the coral specimen and external calibration would be of the order of 0.03%. Differences in density estimates induced by changes in filament age were of the order of 0.10% ($n = 2$ scans). These results are consistent with further unpublished experiments [38].

By contrast, scan setting decisions caused the second largest impact of any variable (figures 2a and 4), with differences of up to 12% between minimum and maximum density offsets for scans of the same sample. The magnitude of this variability was dependent on colony bulk density (figure 4) and, as with the calibration sensitivity, lighter/less dense skeletons were more sensitive to setting adjustments and demonstrated the largest range of potential density offsets between scan conditions. The greyscale intensity histograms derived from less dense skeletons were also more left-skewed regardless of selected settings (figure 4; electronic supplementary material, figure S2). Lower beam energy and more permissive beam filtration (e.g. 140 kV and Cu) consistently resulted in more positive density offsets than the same coral scanned with higher beam energy and stronger filtration (e.g. 215 kV and Sn). In a smaller subset of the sample population, where it was possible to maintain consistent instrumental settings without compromising data quality through including both filtering (Sn 1 mm) and a narrow range of X-ray tube voltages (170–190 kV), the average density offset was 0.1 ± 3.1% (1 SD, extended phantom used; $n = 14$ different corals; figure 4b, dark blue circles).

3.4. How sensitive is the µCT density estimate to reconstruction algorithms and image corrections?

Beam hardening correction using manufacturer presets produced clear improvements in image quality by contrast enhancement between high- and low-density regions (figure 5a); however, this correction introduced the largest error in the density estimation (figure 2a, orange points). Acquisitions across a range of different settings for the same specimen ($\bar{x}$ density offset 1.2 ± 2.5%, $n = 9$; figure 5b) were significantly biased towards excessive density when image corrections were applied to the reconstructions ($\bar{x}$ density offset with beam hardening correction 17.2 ± 6.0%; $F_{(1, 22)} = 70$, $p < 0.001$, ANOVA) with significant paired shifts in density offset by +8% to +28% ($t_{(1, 11)} = 15$, $p < 0.001$, paired-t). The application of beam hardening correction also produced higher sensitivity to operational settings (figure 5b).

4. Discussion

The uncertainties associated with skeletal density measurement are rarely reported in publications. Given the increasing application of X-ray CT analysis in the field of marine calcification research, we have completed a rigorous and comprehensive assessment of the sources and magnitude of errors in coral skeletal density measurements by µCT. Our analysis shows that the µCT density estimate for an individual coral is sensitive to multiple factors: the mass, size and density of the specimen (figure 2); the presence of the phantom within the same data acquisition as the sample (figure 3a); the range and regression fit of density calibration standards (figure 3d,e); the µCT system settings used in the data acquisition (figure 4); and the application of image correction algorithms during reconstruction (figure 5). Based on our analyses we make a series of recommendations that will allow researchers to minimise errors and improve reporting of measurement confidence. The recommendations are split into (i) calibration and (ii) operational processes and are followed by a brief justification.

4.1. Calibration recommendations

— Include the density standards in the same acquisition as the coral specimen (i.e. internal calibration).

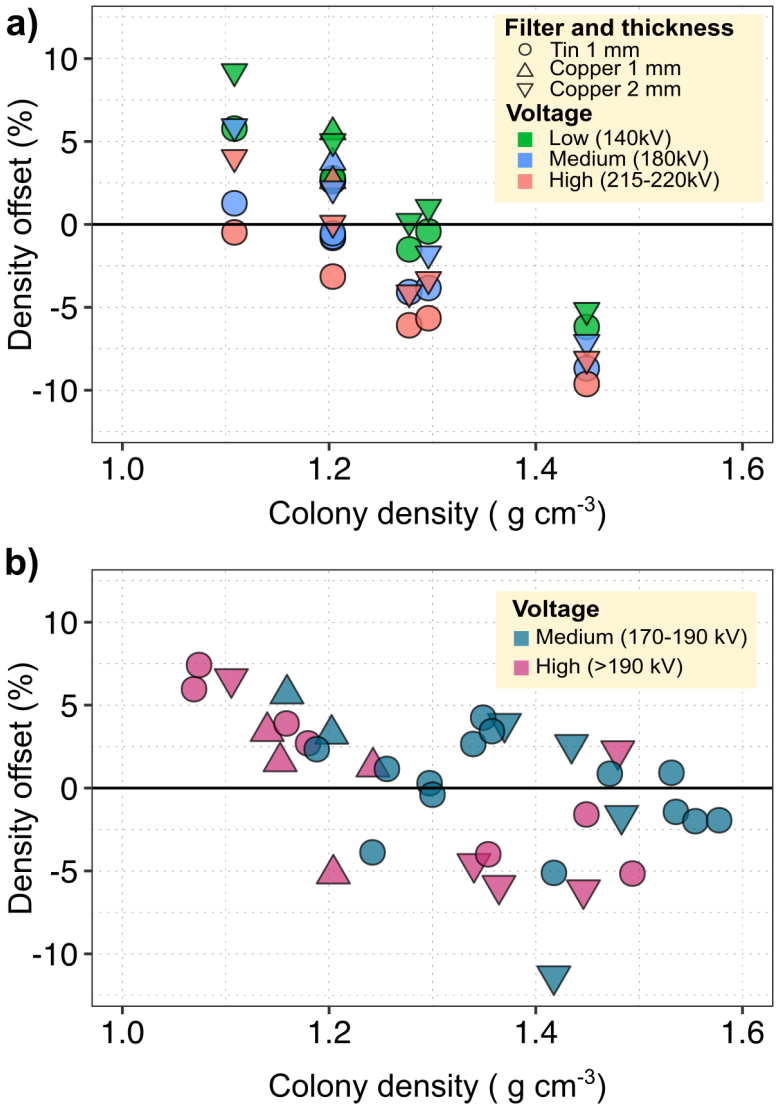

Figure 4. Sensitivity of density estimation to operator-selected system settings in terms of X-ray tube voltage, filter material and thickness**.** (a) Multiple data acquisitions of five specimens under a range of system settings ($n = 5$ to 9 settings). (b) Mean offset for all specimens scanned once with a single set of optimised settings ($n = 36$ specimens).

- Include calibration standards that overlap the maximum extent of the greyscale intensity histogram, with particular care to calibrate the low density extreme and use of 'air' as the lowest density standard.
- Fit the calibration curve with density as the independent variable.

Traditionally, CT calibration standards for coral density analysis have been selected to encompass the expected range of bulk average skeletal densities in the sample set; for example, by using subsampled blocks of coral of a range of bulk densities [29,30] or using commercial phantoms made of epoxy mixed with increasing amounts of calcium hydroxyapatite [14,35]. However, in the worst case scenario we found that more than 50% of an individual coral histogram voxel counts are outside this 'narrow' calibration range (figure 3d). Consequently, using such a 'narrow' range of calibration standards introduces a large calibration-related error (up to 8% shift in bulk density estimate). Additional standards are needed to constrain calibration curves particularly at the low density end of the greyscale histogram, and this is especially critical for the lowest density specimens (figure 2a). At a minimum, simply adding 'air' as a standard (dashed lines in figure 3d,e) approximates the 'extended' phantom regression fits in the density range 0–1.0 g cm^{-3} (solid lines in figure 3d,e). However, the addition of a further range of low density materials mimicking organic components naturally found in coral skeletons increases the confidence in a linear response relationship between density and greyscale intensity. Calibration extension at the upper limits (i.e. beyond densities of 2.0 g cm^{-3}) only

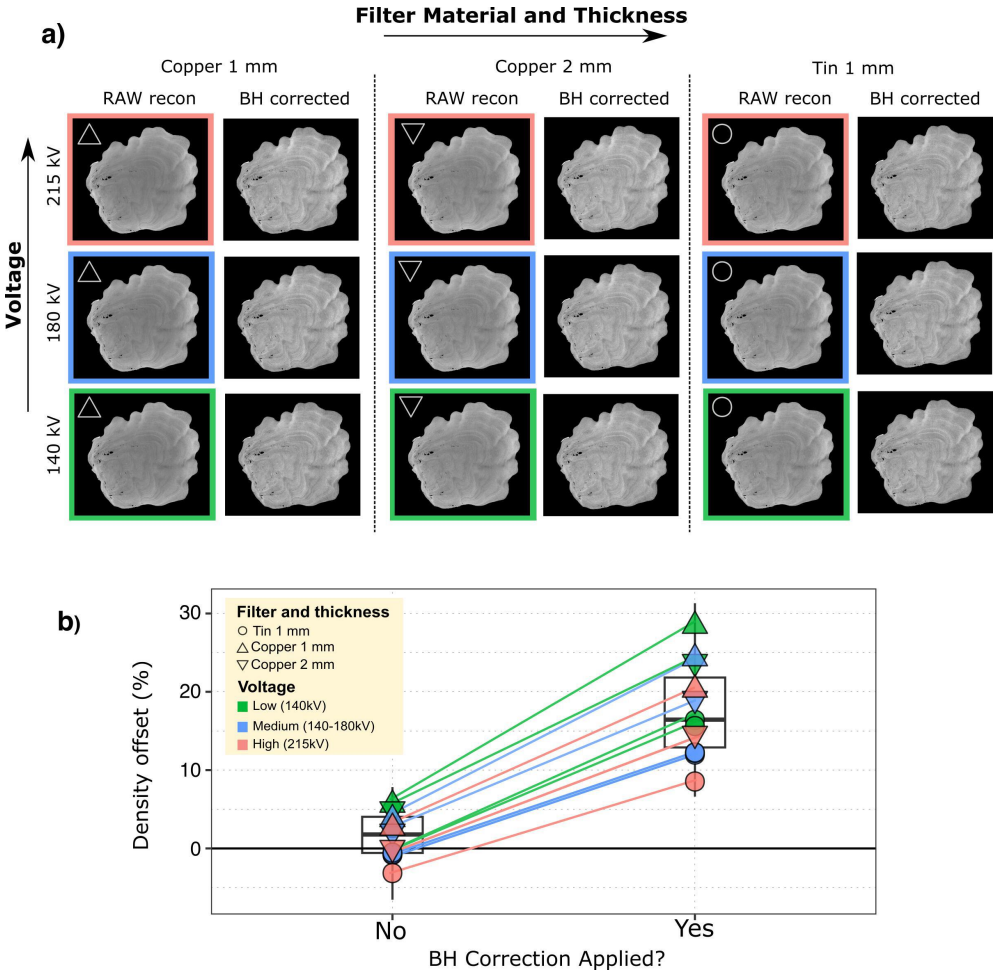

Figure 5. Sensitivity of density estimation to beam hardening correction**.** (a) Reconstructions of the same X-ray µCT slice from a single coral, acquired under nine different operational settings and two post-processing reconstructions ('RAW' and 'BH-corrected'). No image correction was used for 'RAW recon' data reconstructions; Nikon proprietary beam hardening correction algorithm was used in 'BH corrected' reconstructions. (b) Coupled effects of beam hardening correction and operator-selected system settings on the density offset between paired reconstructions with and without the beam hardening (BH) correction applied. The data are also displayed as a boxplot for the population of repeated scans depending on reconstruction treatment.

becomes important for analyses of relatively dense skeletons or specimens that feature dense calcifying structures in addition to the coral matrix (e.g. worm tubes, bivalve and barnacle shells, stress bands, subsumed reef rock and metallic materials; figure 1), where voxel counts could be relatively high beyond the highest standard density point (figure 3e and unshaded histogram region at greyscale intensities >45 000).

4.2. Operational recommendations

- Select optimal scan settings based on X-ray attenuations through the specimen which are indicative of acceptable flux at the detector panel, using appropriate filtering to reduce beam hardening.
- Do not apply any image corrections for beam hardening when reconstructing the three-dimensional volume to extract greyscale intensity for density. Additional volumes reconstructed with proprietary image corrections that increase contrast can still be valuable for other research purposes (e.g. for improved visualization of annual density-banding for growth extension measurements and sclerochronology purposes, or ease of volume segmentation), but must not be used for densitometry.
- Complete a 'bulk mass test' on every specimen scanned by physically weighing the sample to compare with the µCT-derived mass calculated from the distribution of greyscale intensities

(see §2). The bulk 'density offset' quantifies laboratory process error and any scaling correction, if required, for the specific acquisition. This density offset data are invaluable for laboratory monitoring and minimizing errors, as well as essential for reporting the uncertainties associated with the μCT-derived density data.

— Do not apply population-based corrections to density estimates. The density offset is specific to (i) the system settings for the data acquisition and (ii) the individual sample characteristics. Therefore, corrections can only be applied using the respective bulk mass test (bulk specimen density offset) for each acquisition dataset.

System settings, including X-ray tube voltage and current, and X-ray filter materials, are tuned by the μCT operator to optimise the data acquisition and maintain acceptable X-ray fluxes through the densest and thicker parts of a specimen. Various operational solutions are possible and can produce similar outcomes in terms of image quality (figure 5a) but produce a significant spread of density estimates for the same colony (range of bulk density estimates up to approximately 10%; figure 4a). There is a consistent pattern with the most positive density offsets for each coral typically associated with settings of the lowest voltage (140 kV) and Cu filtering, and the most negative value with highest voltage (215 kV) and Sn filtering. While sensitivity to operational settings is expected [33], we show that there is a specimen density and size control that contributes to the magnitude of the impact (figure 4b). Following all our recommendations but selecting a limited subset of specimens with restricted physical characteristics (n = 14), so that we could apply similar voltage (±10 kV) and a single filter choice (Sn 1 mm; dark green circles in figure 4b), the average density offset was reduced to 0.1 ± 3.1% ($\bar{x}$ ± 1 SD) compared with 0.2 ± 4.6% (n = 41) for the full population of samples in our study. However, such restricted system settings are not possible in many studies because operational decisions, including filtering, voltage and current, necessarily vary depending on internal features, and specimen density, size and shape. The need for individualised system tuning to optimise the quality of each scan adds to the importance of continuous density offset monitoring of every sample through any experiment or study.

In some studies, a further correction has been applied across a batch of datasets to correct for a population bias [14,34] and so it is useful to explore how corrections might be applied. It is clear from our large experiment (41 coral specimens internally calibrated in 72 individual μCT acquisitions) that a single common correction determined from the population average cannot reconcile the sources of variability evident between acquisitions and samples. Divergent density offsets are present between scans performed under the same system settings because the bias in response is specimen specific (controlled by density and size). Additionally, in figure 6 for example, we show that forcing the bulk average density offset of multiple data acquisitions of the same sample to 0% requires corrections that vary between +10% and +5% for the densest coral and +1% and −9% for the least dense coral (figure 6a). Any corrections must be applied on an individual scan basis, using derived bulk density offsets for the specific acquisition on the specific sample. Given that the ability to resolve internal density variation in three-dimensional space is the unique advantage of μCT densitometry over other methods (e.g. one- and two-dimensional γ-densitometry), a key follow-on question is whether scaling the dataset (i.e. applying a correction based on the bulk density offset specific to the acquisition) introduces anomalies in internal density estimates for parts of the skeleton at either end of the density range. We demonstrate that this is not a problem by showing that the bulk scaling is equally applicable within selected regions of low- and high-density skeleton (figure 6c,d). In two specimens with very different bulk densities, even the estimates for the most extreme internal densities (figure 6b; □ and ◊ regions of interest) converged after the bulk density offset correction was applied (figure 6c; ±2.3% compared with figure 6d; ±0.8%, ±1 SD).

5. Conclusions

With the rapid advancements in μCT hardware and image reconstruction algorithms [36] and as more research institutions establish μCT research facilities, it is timely to standardise methodology to routinely evaluate the accuracy and precision of densitometry. Here, we have completed a rigorous and comprehensive assessment of the scale and types of analytical errors in coral skeletal density

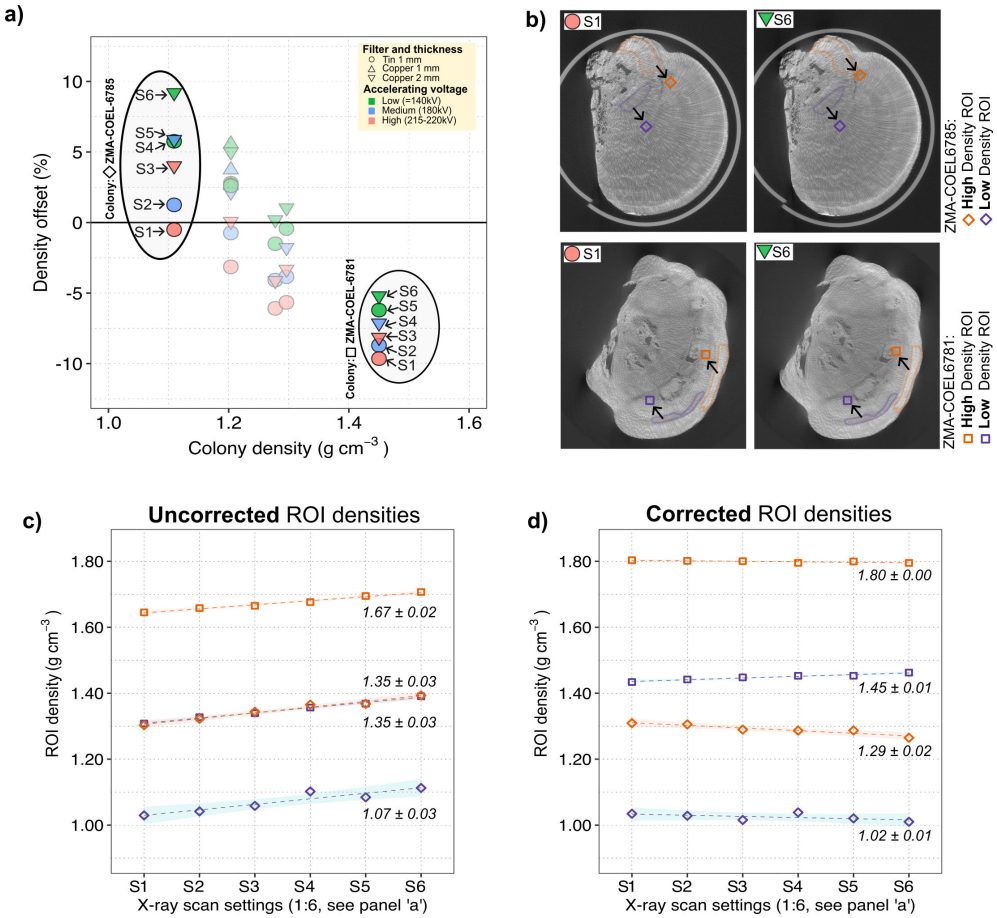

Figure 6. The influence of whole specimen density corrections on specific regions of interest (ROIs) within a specimen. (a) Bulk density offsets from multiple scans under a range of optimal instrument settings (S1 to S6) highlighted for two coral specimens (◊ and □ in following panels). (b) Example µCT reconstructed slice under scan settings S1 and S6, with low- and high-density ROIs (purple and orange respectively) outlined in the two specimens. (c) µCT density estimate for the four ROIs across six different scan settings (mean density ± 1 SD values shown in g cm^{-3}). (d) Individual ROI densities as for (c) but with bulk density offset correction applied.

measurements by µCT using the largest population of coral analysed to date. We also develop a simple, yet robust approach to quantify the accuracy and precision of µCT density estimates as the relative percent offset between virtual µCT-derived and actual specimen masses. We demonstrate that µCT-derived density estimates are sensitive to (in descending order of impact): (i) image post-processing for beam hardening correction, (ii) operator-selected µCT system settings including voltage and filtering, (iii) the size and internal density variations of the specimen, and (iv) density calibration aspects, including standard density range, regression analysis and whether the phantom is scanned within the same acquisition as the sample. Of all potential sources of uncertainty, instrumental noise is insignificant (<0.1%). Although we show that some of these sources of error and variability can be minimised or avoided, operational system decisions tailored to specimen size, shape and internal density structures must be monitored and reported.

We demonstrate that accurate µCT density estimates can be produced by following the calibration and operational recommendations outlined above. In our study of 41 *Porites* spp. coral with a broad range of bulk average skeletal densities (1.07–1.57 g m^{-3}) and mass (87.9–2176.5 g), the population mean density offset between the µCT-derived and actual value was 0.2 ± 4.6% ($\bar{x}$ ± 1 SD, n = 41). Although the measurement uncertainty is considerably smaller than the signal response in coral skeletal density variations reported across different environmental conditions and reefs, the systematic bias related to bulk density and sample mass still needs to be assessed and corrected. The practical and simple bulk mass test protocol will assist researchers in assessing the accuracy of skeletal density estimates from µCT datasets and this assessment should be completed as standard laboratory practice for monitoring and data reporting. Standard reporting of accuracy and precision is essential for

continued optimization and confidence in these data and will advance our understanding of the effect of environmental and climate change on marine calcifying organisms.

Ethics. This work did not require ethical approval from a human subject or animal welfare committee.

Data accessibility. Data and relevant code for this research work are stored in GitHub: https://github.com/LeoBertini/CoralMethodsPaper and have been archived within the Zenodo repository [46]. Supplementary results and tables are also provided as part of the electronic supplementary material [47].

Declaration of AI use. We have not used AI-assisted technologies in creating this article.

Authors' contributions. L.B.: conceptualization, data curation, formal analysis, funding acquisition, investigation, methodology, project administration, resources, software, validation, visualization, writing—original draft, writing—review and editing; E.H.: conceptualization, formal analysis, funding acquisition, investigation, methodology, project administration, resources, supervision, validation, visualization, writing—original draft, writing—review and editing; R.S.: investigation, validation, writing—review and editing; V.F.: data curation, formal analysis, investigation, methodology, resources, validation, writing—original draft, writing—review and editing; B.C.: data curation, investigation, resources, validation, writing—review and editing; E.M.-S.: data curation, investigation, resources, validation, writing—review and editing; F.L.: data curation, investigation, resources, supervision, validation, writing—review and editing; M.B.K.: data curation, investigation, methodology, resources, validation, writing—review and editing; K.J.: conceptualization, funding acquisition, investigation, methodology, project administration, resources, software, supervision, validation, visualization, writing—review and editing.

All authors gave final approval for publication and agreed to be held accountable for the work performed therein.

Conflict of interest declaration. We declare we have no competing interests.

Funding. Support for L.B. and this study is acknowledged through 4D-REEF, a Marie Skłodowska-Curie Innovative Training Network funded by European Union Horizon 2020 research and innovation programme under grant agreement number 813360. We are also grateful for additional support from SYNTHESIS+ Transnational Access project NL-TAF-TA3-009 and the Natural History Museum Science Investment Fund and the University of Bristol Covid Recovery Fund.

Acknowledgements. The authors would like to thank the NHM curatorial team, especially Jill Darrell, Brian Rosen and Miranda Lowe for facilitating access to specimens. We would also like to thank colleagues from the Naturalis Biodiversity Centre, who hosted L.B. and facilitated access to the coral collection through the SYNTHESIS+ initiative, in particular Willem Renema, Hannco Bakker and colleagues who assisted with the selection and shipping of loan specimens to the NHM, Bram van der Bijl, Jeroen Goud, Bert Hoeksema and Wendy van Bohemen, as well as the μCT technicians Rob Langelaan and Bertie Joan van Heuven. L.B. would also like to thank colleagues from the School of Earth Sciences at the University of Bristol, Claudia Hildebrant and Tim Tomkinson for the calcite and aragonite samples in the mineral collection as well as Charles Clapham and Gerald Mwale for mineral preparation in the workshop. L.B. would also like to thank Dan Lunt, Richard Brooker, Philip Donoghue and Tilo Burghardt for valuable discussions. The authors gratefully acknowledge the anonymous reviewers for their encouraging and constructive comments.

References

1. Hatcher BG. 1997 Coral reef ecosystems: how much greater is the whole than the sum of the parts? *Coral Reefs* **16**, S77–S91. (doi:10.1007/s003380050244)
2. Vecsei A. 2004 A new estimate of global reefal carbonate production including the fore-reefs. *Glob. Planet. Chang.* **43**, 1–18. (doi:10.1016/j.gloplacha.2003.12.002)
3. Cornwall CE *et al*. 2021 Global declines in coral reef calcium carbonate production under ocean acidification and warming. *Proc. Natl Acad. Sci. USA* **118**, e2015265118. (doi:10.1073/pnas.2015265118)
4. Molina-Hernández A, González-Barrios FJ, Perry CT, Álvarez-Filip L. 2020 Two decades of carbonate budget change on shifted coral reef assemblages: are these reefs being locked into low net budget states? *Proc. R. Soc. B* **287**, 20202305. (doi:10.1098/rspb.2020.2305)
5. Chave KE, Smith SV, Roy KJ. 1972 Carbonate production by coral reefs. *Mar. Geol.* **12**, 123–140. (doi:10.1016/0025-3227(72)90024-2)
6. Lange ID, Perry CT, Alvarez-Filip L. 2020 Carbonate budgets as indicators of functional reef 'health': a critical review of data underpinning census-based methods and current knowledge gaps. *Ecol. Indic.* **110**, 105857. (doi:10.1016/j.ecolind.2019.105857)
7. Lough JM, Barnes DJ. 1992 Comparisons of skeletal density variations in Porites from the central Great Barrier Reef. *J. Exp. Mar. Biol. Ecol.* **155**, 1–25. (doi:10.1016/0022-0981(92)90024-5)
8. Pratchett MS, Anderson KD, Hoogenboom MO, Widman E, Baird AH, Pandolfi JM, Edmunds PJ, Lough JM. 2015 Spatial, temporal and taxonomic variation in coral growth—implications for the structure and function of coral reef ecosystems. *Oceanogr. Mar. Biol. Annu. Rev.* **53**, 215–295. (doi:10.1201/b18733)
9. Lough JM, Barnes DJ. 2000 Environmental controls on growth of the massive coral Porites. *J. Exp. Mar. Biol. Ecol.* **245**, 225–243. (doi:10.1016/s0022-0981(99)00168-9)

10. Lough JM, Barnes DJ. 1997 Several centuries of variation in skeletal extension, density and calcification in massive *Porites* colonies from the Great Barrier Reef: a proxy for seawater temperature and a background of variability against which to identify unnatural change. *J. Exp. Mar. Biol. Ecol.* **211**, 29–67. (doi:10.1016/s0022-0981(96)02710-4)
11. Spencer Davies P. 1989 Short-term growth measurements of corals using an accurate buoyant weighing technique. *Mar. Biol.* **101**, 389–395. (doi:10.1007/bf00428135)
12. Bucher DJ, Harriott VJ, Roberts LG. 1998 Skeletal micro-density, porosity and bulk density of acroporid corals. *J. Exp. Mar. Biol. Ecol.* **228**, 117–136. (doi:10.1016/s0022-0981(98)00020-3)
13. Dodge RE, Wyers SC, Frith HR, Knap AH, Smith SR, Cook CB, Sleeter TD. 1984 Coral calcification rates by the buoyant weight technique: effects of alizarin staining. *J. Exp. Mar. Biol. Ecol.* **75**, 217–232. (doi:10.1016/0022-0981(84)90167-9)
14. Carilli JE, Hartmann AC, Heron SF, Pandolfi JM, Cobb K, Sayani H, Dunbar R, Sandin SA. 2017 *Porites* coral response to an oceanographic and human impact gradient in the Line Islands. *Limnol. Oceanogr.* **62**, 2850–2863. (doi:10.1002/lno.10670)
15. Barnes DJ, Devereux MJ. 1988 Variations in skeletal architecture associated with density banding in the hard coral *Porites*. *J. Exp. Mar. Biol. Ecol.* **121**, 37–54. (doi:10.1016/0022-0981(88)90022-6)
16. Knutson DW, Buddemeier RW, Smith SV. 1972 Coral chronometers: seasonal growth bands in reef corals. *Science* **177**, 270–272. (doi:10.1126/science.177.4045.270)
17. Buddemeier RW, Maragos JE, Knutson DW. 1974 Radiographic studies of reef coral exoskeletons: rates and patterns of coral growth. *J. Exp. Mar. Biol. Ecol.* **14**, 179–199. (doi:10.1016/0022-0981(74)90024-0)
18. Hudson JH. 1981 Growth rates in *Montastraea annularis*: a record of environmental change in Key Largo Coral Reef Marine Sanctuary, Florida. *Bull. Mar. Sci.* **31**, 444–459.
19. Chalker B, Barnes D, Isdale P. 1985 Calibration of x-ray densitometry for the measurement of coral skeletal density. *Coral Reefs* **4**, 95–100. (doi:10.1007/BF00300867)
20. Dodge RE, Thomson J. 1974 The natural radiochemical and growth records in contemporary hermatypic corals from the Atlantic and Caribbean. *Earth Planet. Sci. Lett.* **23**, 313–322. (doi:10.1016/0012-821X(74)90121-6)
21. Carricart-Ganivet JP, Barnes DJ. 2007 Densitometry from digitized images of X-radiographs: methodology for measurement of coral skeletal density. *J. Exp. Mar. Biol. Ecol.* **344**, 67–72. (doi:10.1016/j.jembe.2006.12.018)
22. Rico-Esenaro SD, Sanchez-Cabeza JA, Carricart-Ganivet JP, Montagna P, Ruiz-Fernández AC. 2019 Uncertainty and variability of extension rate, density and calcification rate of a hermatypic coral (*Orbicella faveolata*). *Sci. Total Environ.* **650**, 1576–1581. (doi:10.1016/j.scitotenv.2018.08.397)
23. Chalker BE, Barnes DJ. 1990 Gamma densitometry for the measurement of skeletal density. *Coral Reefs* **9**, 11–23. (doi:10.1007/bf00686717)
24. Lough JM, Barnes DJ. 1990 Intra-annual timing of density band formation of *Porites* coral from the central Great Barrier Reef. *J. Exp. Mar. Biol. Ecol.* **135**, 35–57. (doi:10.1016/0022-0981(90)90197-k)
25. Cooper TF, De'ath G, Fabricius KE, Lough JM. 2008 Declining coral calcification in massive *Porites* in two nearshore regions of the northern Great Barrier Reef. *Glob. Chang. Biol.* **14**, 529–538. (doi:10.1111/j.1365-2486.2007.01520.x)
26. Zoppe SF, Deveaux M, Gischler E. 2022 Quantifying skeletal density at high temporal resolution in massive scleractinian corals by using two-dimensional grid-scanning gamma densitometry. *Geo-Mar. Lett.* **42**, 16. (doi:10.1007/s00367-022-00739-6)
27. Duprey N, Boucher H, Jiménez C. 2012 Digital correction of computed X-radiographs for coral densitometry. *J. Exp. Mar. Biol. Ecol.* **438**, 84–92. (doi:10.1016/j.jembe.2012.09.007)
28. Bosscher H. 1993 Computerized tomography and skeletal density of coral skeletons. *Coral Reefs* **12**, 97–103. (doi:10.1007/bf00302109)
29. DeCarlo TM, Cohen AL, Barkley HC, Cobban Q, Young C, Shamberger KE, Brainard RE, Golbuu Y. 2015 Coral macrobioerosion is accelerated by ocean acidification and nutrients. *Geology* **43**, 7–10. (doi:10.1130/G36147.1)
30. DeCarlo TM, Cohen AL. 2017 Dissepiments, density bands and signatures of thermal stress in *Porites* skeletons. *Coral Reefs* **36**, 749–761. (doi:10.1007/s00338-017-1566-9)
31. Helmle KP, Dodge RE, Ketcham R. 2000 Skeletal architecture and density banding in *Diploria strigosa* by X-ray computed tomography. In *Proc. 9th Int. Coral Reef Symp., Bali, Indonesia, 23–27 October 2000*, pp. 365–371.
32. Carilli J, Donner SD, Hartmann AC. 2012 Historical temperature variability affects coral response to heat stress. *PLoS One* **7**, e34418. (doi:10.1371/journal.pone.0034418)
33. DeCarlo TM. 2017 Deriving coral skeletal density from computed tomography (CT): effects of scan and reconstruction settings. *Matters Select* **3**, e201706000005. (doi:10.19185/matters.201706000005)
34. Chan P, Halfar J, Norley CJD, Pollmann SI, Adey W, Holdsworth DW. 2017 Micro-computed tomography: applications for high-resolution skeletal density determinations: an example using annually banded crustose coralline algae. *Geochem. Geophys. Geosyst.* **18**, 3542–3553. (doi:10.1002/2017GC006966)
35. Cantin NE, Cohen AL, Karnauskas KB, Tarrant AM, McCorkle DC. 2010 Ocean warming slows coral growth in the central Red Sea. *Science* **329**, 322–325. (doi:10.1126/science.1190182)
36. Coban SB, Lucka F, Palenstijn WJ, Van Loo D, Batenburg KJ. 2020 Explorative imaging and its implementation at the FleX-ray laboratory. *J. Imaging* **6**, 18. (doi:10.3390/jimaging6040018)
37. Lough JM, Cantin NE. 2014 Perspectives on massive coral growth rates in a changing ocean. *Biol. Bull.* **226**, 187–202. (doi:10.1086/bblv226n3p187)
38. Summerfield R. 2021 Baselines of growth and stress from massive corals in the Chagos archipelago. PhD thesis, University of Bristol, UK.

39. Ning R, Tang X, Conover D. 2004 X-ray scatter correction algorithm for cone beam CT imaging. *Med. Phys.* **31**, 1195–1202. (doi:10.1118/1.1711475)
40. Liu W, Rong J, Gao P, Liao Q, Lu H. 2016 Algorithm for x-ray beam hardening and scatter correction in low-dose cone-beam CT: phantom studies. In *Proc. SPIE 9783, Medical Imaging 2016: Physics of Medical Imaging*, p. 978332. SPIE Medical Imaging: San Diego, CA. (doi:10.1117/12.2217424)
41. Davis GR. 2022 Development of two-dimensional beam hardening correction for X-ray micro-CT. *J. X Ray Sci. Technol.* **30**, 863–874. (doi:10.3233/xst-221178)
42. Barrett JF, Keat N. 2004 Artifacts in CT: recognition and avoidance. *RadioGraphics* **24**, 1679–1691. (doi:10.1148/rg.246045065)
43. Withers PJ *et al*. 2021 X-ray computed tomography. *Nat. Rev. Methods Primers* **1**, 18. (doi:10.1038/s43586-021-00015-4)
44. Hsieh J, Flohr T. 2021 Computed tomography recent history and future perspectives. *J. Med. Imaging* **8**, 052109. (doi:10.1117/1.jmi.8.5.052109)
45. Hsieh J. 2015 *Computed tomography: principles, design, artifacts, and recent advances*, 3rd edn. Bellingham, WA: SPIE Press. (doi:10.1117/3.2197756)
46. LB. 2024 How to quantify and minimise error in coral skeletal density estimates using X-ray µCT (2.1). Zenodo. (doi:10.5281/zenodo.14497610)
47. Bertini L *et al*. 2026 Supplementary material from: How to quantify and minimise error in coral skeletal density estimates using X-ray µCT. Figshare. (doi:10.6084/m9.figshare.c.8335609)